J Nanopart Res (2017) 19:191
DOI 10.1007/s11051-017-3895-6

RESEARCH PAPER

# HRTEM analyses of the platinum nanoparticles prepared on graphite particles using coaxial arc plasma deposition

**Kun'ichi Miyazawa · Masaru Yoshitake · Yumi Tanaka**

Received: 27 February 2017 / Accepted: 17 May 2017


**Abstract** Platinum nanoparticles with diameters less than ~5 nm were prepared on graphite particles by the coaxial arc plasma deposition, and the structure of platinum nanoparticles was investigated using high-resolution transmission electron microscopy. {110} facets of platinum nanoparticles parallel to the surface (0001) planes of graphite particles were most frequently observed. The platinum nanoparticles were found to be anisotropically deformed from the bulk face-centered cubic structure, and the lattice parameters of platinum nanoparticles were estimated by assuming monoclinic structures. No correlation was observed between the diameter and the lattice parameters of the platinum nanoparticles. Approximately two-thirds of the platinum nanoparticles were compressively strained, and the other platinum nanoparticles showed the expanded unit cells. The cube root of monoclinic unit cell of the platinum nanoparticles varied from a compression of 5.9% to an expansion of 2.8% as compared with the bulk lattice constant of platinum.

**Keywords** Platinum nanoparticle · CAPD · HRTEM · Graphite · Structure · Catalytic effect

K. Miyazawa (✉) · M. Yoshitake · Y. Tanaka
Department of Industrial Chemistry, Faculty of Engineering, Tokyo University of Science, Tokyo 162-0826, Japan
e-mail: miyakuni@rs.tus.ac.jp

## Introduction

Platinum (Pt) and Pt alloy nanoparticles (NPs) are the most widely used catalysts for the polymer electrolyte fuel cells (Sepp et al. 2016; Miyabayashi and Miyake 2016). It has been reported that the oxygen reduction activity of Pt NPs depends on their size and becomes maximum for the particle size of 2.2 nm (Shao et al. 2011). On the other hand, it has been reported that the lattice constant of carbon-supported Pt NPs with the face-centered cubic (fcc) structure was smaller than that of bulk Pt and decreased with decreasing diameter and that this phenomenon became pronounced for the diameters less than about 10 nm, using X-ray diffraction method (Leontyev et al. 2014). The decrease of lattice constant of fcc Pt NPs with decreasing diameter was also reported through researches using transmission electron microscopy (TEM). For example, the lattice constant of Pt NPs was measured using electron diffraction spots (Solliard and Flueli 1985), or it was measured using the Moiré patterns that were formed between Pt NPs and $Al_2O_3$ substrates (Klimenkov et al. 1997). In the case of palladium (Pd) which is used for the exhaust gas catalyst (Gholami et al. 2015) and is an indispensable element for the Pd-Pt core-shell catalysts in polymer electrolyte fuel cells (Khatee et al. 2016), the reduction of lattice constant with decreasing the particle size was also reported in Pd NPs by Lamber et al. (1995).

Numerous papers have been published for the relationship between the lattice constant and the crystal size until

Published online: 29 May 2017

today. The study about the variation of lattice constant depending on the crystal size can be traced back to the paper by Finch and Fordham (1936). They showed that the lattice constants of ZnO and alkali halides (lithium, sodium, and potassium halides) varied depending on their sizes, using electron diffraction. Fifteen years later, Boswell (1951) showed the decrease of lattice constant of alkali halide NPs (NaCl, KCl, NaBr, LiF) and gold NPs with decreasing their size, using electron diffraction. The reduction of lattice constant with decreasing the size of small crystals was discussed in relation with the surface compressive layers in the case of NaCl crystals (Boswell 1951), referring the theory of by Lennard-Jones and Dent (1928) who calculated the surface tension of NaCl-type crystals that affects the interatomic distances of crystal surfaces. Further, the reduction of lattice parameter with decreasing the crystal size by use of electron diffraction was reported for silver nanocrystals by Berry (1952). The reduction of lattice parameter of NPs has been explained by the surface tension that becomes more apparent with decreasing their crystal size (Berry 1952; Leontyev et al. 2014; Qi et al. 2009). In the synchrotron XRD measurements of the Pt NPs prepared on carbon supports, the lattice constant of Pt NPs was always lower than that of bulk Pt (Leontyev et al. 2014; Birringer and Zimmer 2009).

Mavrikakis et al. (1998) reported that the surface strain of metals shifts the d band center of metals and varies the catalytic activity of metals, based on the study of self-consistent density functional calculations in the interaction among oxygen, CO and Ru (0001) surfaces, and that surface strain can in general be used to tailor the catalytic activity of metals. Later, Wang et al. (2009) reported that the oxygen reduction reaction (ORR) activity is enhanced in the contracted Pt surface layers and that, referring the volcano plots by Zhang et al. (2005), moderate compressive strain in the Pt surface layer enhances the ORR activity. Recently, Daio et al. (2015) reported the localized strain on Pt NPs that changes depending on the kind of substrates using carbon black and $SnO_2$.

As described above, the size-dependent variation of lattice constant and the lattice strain of Pt NPs are very important factors that must be considered in preparing efficient catalysts in polymer electrolyte fuel cells. Among various preparation methods of metal NPs, the coaxial arc plasma deposition (CAPD) has been developed recently as a simple dry process that can directly prepare metal NPs on substrates in vacuum (Agawa et al. 2015). Preparation of Pt NPs has been performed using CAPD, and their microstructure observations by TEM have been reported (Agawa et al. 2015; Hinokuma et al. 2009). The structural analysis of the Pt NPs prepared by CAPD, however, has not been conducted in atomic scale so far. Using the high-resolution transmission electron microscopy (HRTEM), we have investigated the atomic structure of the Pt NPs prepared on graphite particles by CAPD and have found the Pt NPs anisotropically distorted from the fcc symmetry of bulk Pt. This paper reports the detailed structural characteristics of the Pt NPs prepared by CAPD.

## Experimental

Pt NPs were deposited on as-received graphite particles (GNH-XZ, Graphene Platform Corp, Tokyo, Japan) using a coaxial arc plasma deposition (CAPD) source (APD-1P, ADVANCE RIKO, Inc., Yokohama, Japan) with a condenser capacity of 720 μF and a discharge voltage of 100 V under vacuum using a turbomolecular pumping system (Agawa et al. 2015).

The magnification of TEM (JEOL JEM-2800, 200 kV, Tokyo, Japan) was calibrated using lattice images of high-purity silicon crystals (Optostar Ltd., Tsukuba, Japan).

The diameter of a Pt NP was estimated using the circle having the same area with the Pt NP, measuring the binary image area of the Pt NP, where image analysis software packages of HALCON (MVTec Software GmbH, Munich, Germany) and Adobe Photoshop CS6 were used. The simulation of HRTEM images was conducted using the self-developed software based on the eigenvalue method (Miyazawa et al. 2001).

## Results and discussion

Microstructural examples of graphite particles used for Pt deposition are shown in Fig. 1. Various sizes of graphite particles as shown in Fig. 1a ranging from a few hundred nanometers to sizes greater than 1 μm were observed. Figure 1b, c shows HRTEM images for parts of graphite particles with sheet thicknesses of 3.6 and 8.6 nm, respectively. Figure 1d shows a scanning transmission electron microscopy (STEM, JEOL JEM-2800) dark field image for a part of graphite particle with a thickness of ~58 nm. The inset image of Fig. 1d shows an enlarged image exhibiting the stacked graphene

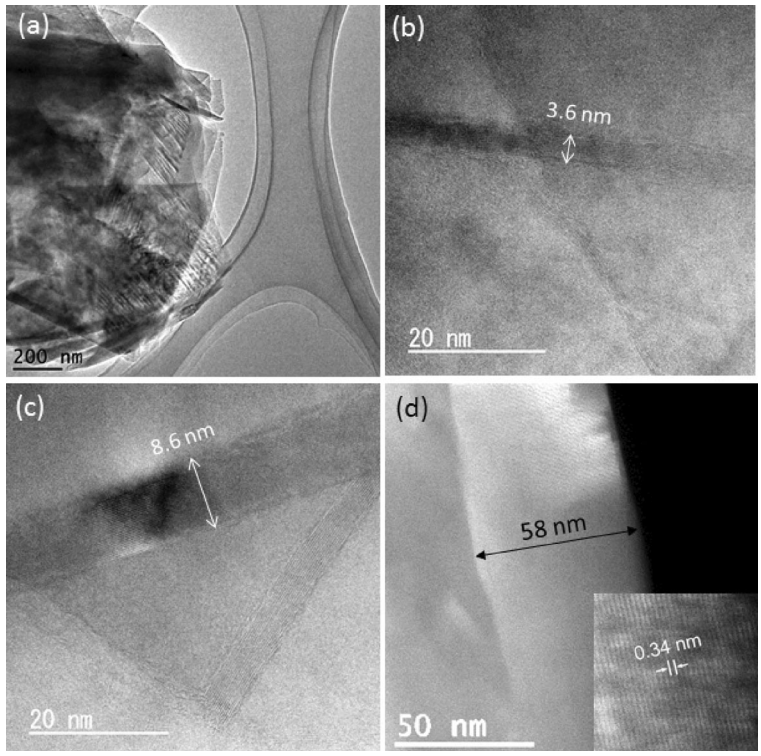


**Fig. 1** TEM image of **a** a graphite particle, **b** part of graphite particle with ~10 layers, and **c** part of graphite particle with ~25 layers. **d** STEM image of a part of graphite particle with ~170 layers, where the *inset* shows an enlarged image of the stacked graphene layers

layers with a spacing of 0.34 nm. The thickness of graphite particles was observed to range from ~10 to ~170 layers.

Figure 2 shows a HRTEM example of Pt NPs deposited on a multilayer graphite particle. The Pt NPs appear to have the flattened morphologies in Fig. 2a and exhibit clear {111} habit planes in Fig. 2e. HRTEM images taken along the zone axes of [001] for particle 1 and $[\bar{1}10]$ for particle 4 are found in Fig. 2b, e. However, most HRTEM images could be obtained under off-axis conditions as shown in Fig. 2c, d, where only {111} and {200} single fringes are resolved.

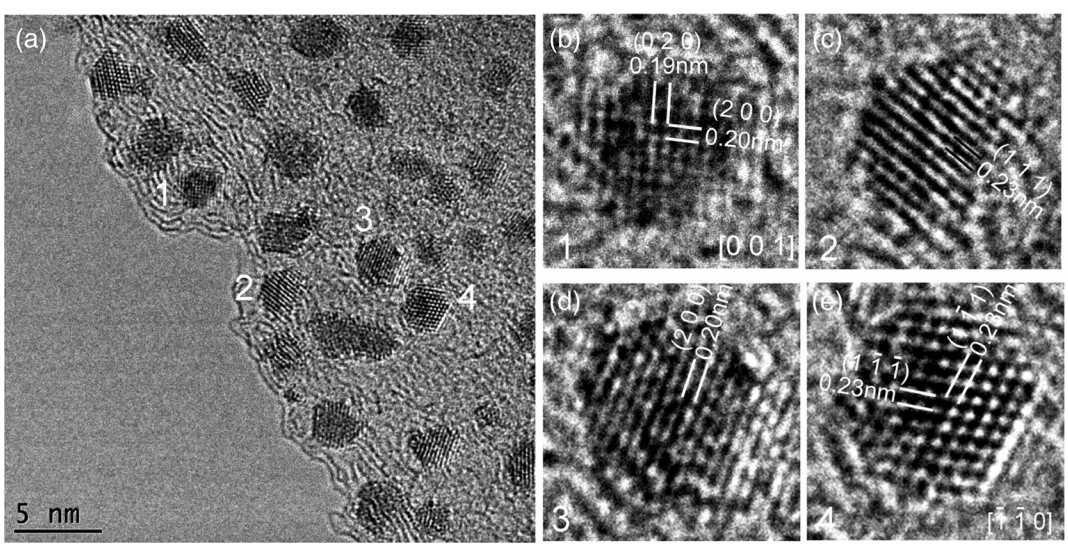


**Fig. 2** HRTEM image **a** of Pt particles deposited on a graphite particle. Enlarged images of particles 1, 2, 3, and 4 are shown in **b**, **c**, **d**, and **e**, respectively

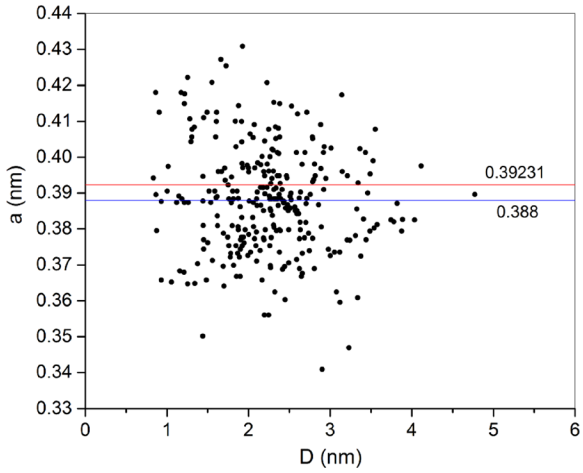


**Fig. 3** Relationship between the diameter *D* (nm) of Pt NPs and the fcc lattice constant a (nm)

The lattice constant of Pt NPs was calculated for the HRTEM images of observed 285 Pt NPs, using {200} or {111} fringes, and equation $a = d_{hkl}(h^2 + k^2 + l^2)^{1/2}$ for a (hkl) plane of face-centered cubic (fcc) structure. The result is shown in Fig. 3 that is plotted as a function of NP diameter.

A very large scattering of *a* is observed, and no correlation can be seen between the lattice constant *a* and the particle diameter *D*. The mean lattice constant for the 285 Pt nanoparticles was calculated to be $a = 0.388 \pm 0.015$ nm (mean ± std), which is smaller by ~1% than the Pt bulk lattice constant $a = 0.39231$ nm (JCPDS 00–004-0802). It is noticed that the dispersion of lattice constant *a* increases as the diameter decreases. The large scattering in the lattice constant *a* indicates that the crystal structure of Pt nanoparticles is anisotropically distorted from the pristine fcc

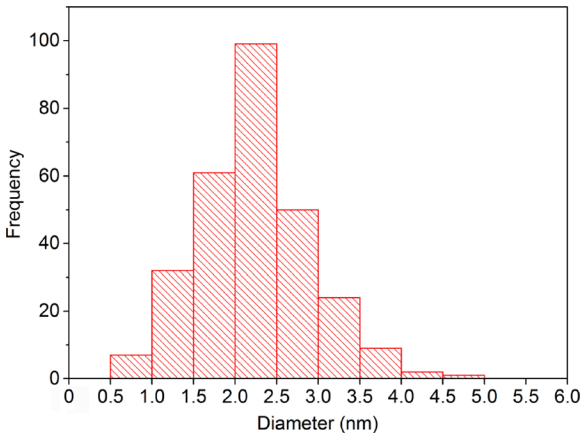


**Fig. 4** Histogram showing the diameter distribution of the 285 Pt NPs deposited on the graphite particles

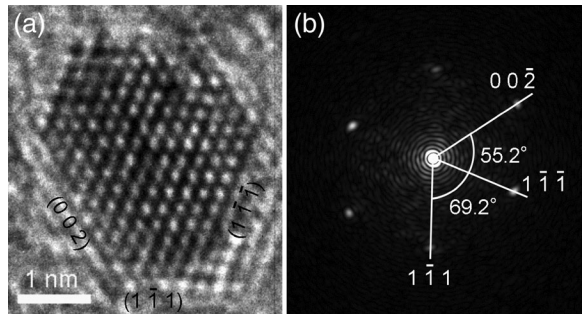


**Fig. 5** **a** HRTEM image of a Pt NP taken along [110] zone axis. **b** FFT pattern for the Pt NP image **a**

crystal structure like the case of Se nanoparticles (Zhang et al. 1995). The anisotropic distortion of unit cell produces non-equivalent {111} or {200} planes with different interplanar spacings, which leads to the variation of lattice constant *a*.

As shown in Fig. 4, the Pt NPs with diameters between 2.0 and 2.5 nm were most frequently observed, where the mean diameter of Pt NPs is 2.2 ± 0.7 nm (Fig. 4). Shao et al. (2011) reported that this size of 2.2 nm exhibited the maximum mass activity of ORR by the Pt NPs in a $HClO_4$ solution.

An example of anisotropic distortion of Pt NP lattice is shown in Fig. 5. Figure 5b shows a fast Fourier transform (FFT) pattern of a Pt NP for Fig. 5a, where the measured interplanar angles are indicated. In pristine fcc crystals, the interplanar angle between {111} and {200} planes is 54.7° and that between two {111} planes is 70.5°. However, the observed angles are deviated from those values. This example shows that the Pt NPs are anisotropically distorted from the pristine fcc lattice.

Hence, in order to obtain more precise lattice parameters, only the on-axis HRTEM images along <110> zone axes were analyzed, assuming monoclinic structures with lattice constants *a*, *b*, *c*, and $\beta$ (axial angle). The analytical method was conducted as follows, using the Pt NP of Fig. 5 for example. The lattice plane spacings $d(1\bar{1}1)$, $d(1\bar{1}\bar{1})$, and $d(002)$ were calculated so that $F(a, b, c, \beta)$ becomes minimum by varying *a*, *b*, *c*, and $\beta$, using Mathematica, where $d_0$(hkl) means the (hkl) interplanar spacing measured from the observed HRTEM image.

$$F(a,b,c,\beta) \equiv \left(d_0\left(1\bar{1}1\right) - d\left(1\bar{1}1\right)\right)^2 + \left(d_0\left(1\bar{1}\bar{1}\right) - d\left(1\bar{1}\bar{1}\right)\right)^2 + \left(d_0(002) - d(002)\right)^2$$

Table 1 shows the optimized lattice parameters and the calculated interplanar spacings. The measured three

**Table 1** Monoclinic lattice parameters estimated by minimizing F(a, b, c, β) for the HRTEM image of Fig. 5a

| Measured $d_0$(hkl) (nm) | | | Optimized lattice parameters | | | | Calculated $d$(hkl) (nm) | | |
|---|---|---|---|---|---|---|---|---|---|
| $(1\bar{1}1)$ | $(1\bar{1}\bar{1})$ | (002) | $a$ (nm) | $b$ (nm) | $c$ (nm) | $\beta$ (°) | $(1\bar{1}1)$ | $(1\bar{1}\bar{1})$ | (002) |
| 0.217 | 0.220 | 0.192 | 0.375 | 0.375 | 0.385 | 90.9 | 0.217 | 0.220 | 0.192 |

interplanar spacings were well fitted by this least square method.

One hundred Pt NPs were observed along <110> zone axes, and the optimized monoclinic lattice parameters were obtained and plotted as a function of Pt NP diameter in Fig. 6. Figure 7 displays the size distribution of the analyzed Pt NPs, where the mean size is 2.9 ± 0.7 nm. As compared with the case of Fig. 4, slightly larger Pt NPs with crossed lattice fringes were analyzed. In Fig. 6, no correlation is observed between the lattice parameters and the particle diameter like the case of Fig. 3. The mean values of lattice parameters are $a$ = 0.381 ± 0.012 nm, $b$ = 0.383 ± 0.012 nm, $c$ = 0.397 ± 0.021 nm, and $\beta$ = 93.2 ± 2.1°. The wide variation of lattice constants indicates that the Pt NPs are randomly distorted irrespective of particle size. Parameter $\beta$ is a measure for shear strain. The observed different shear strains are presumed to be originated from different magnitudes of interaction between Pt and carbon atoms at the Pt-graphite particle joint interfaces. The

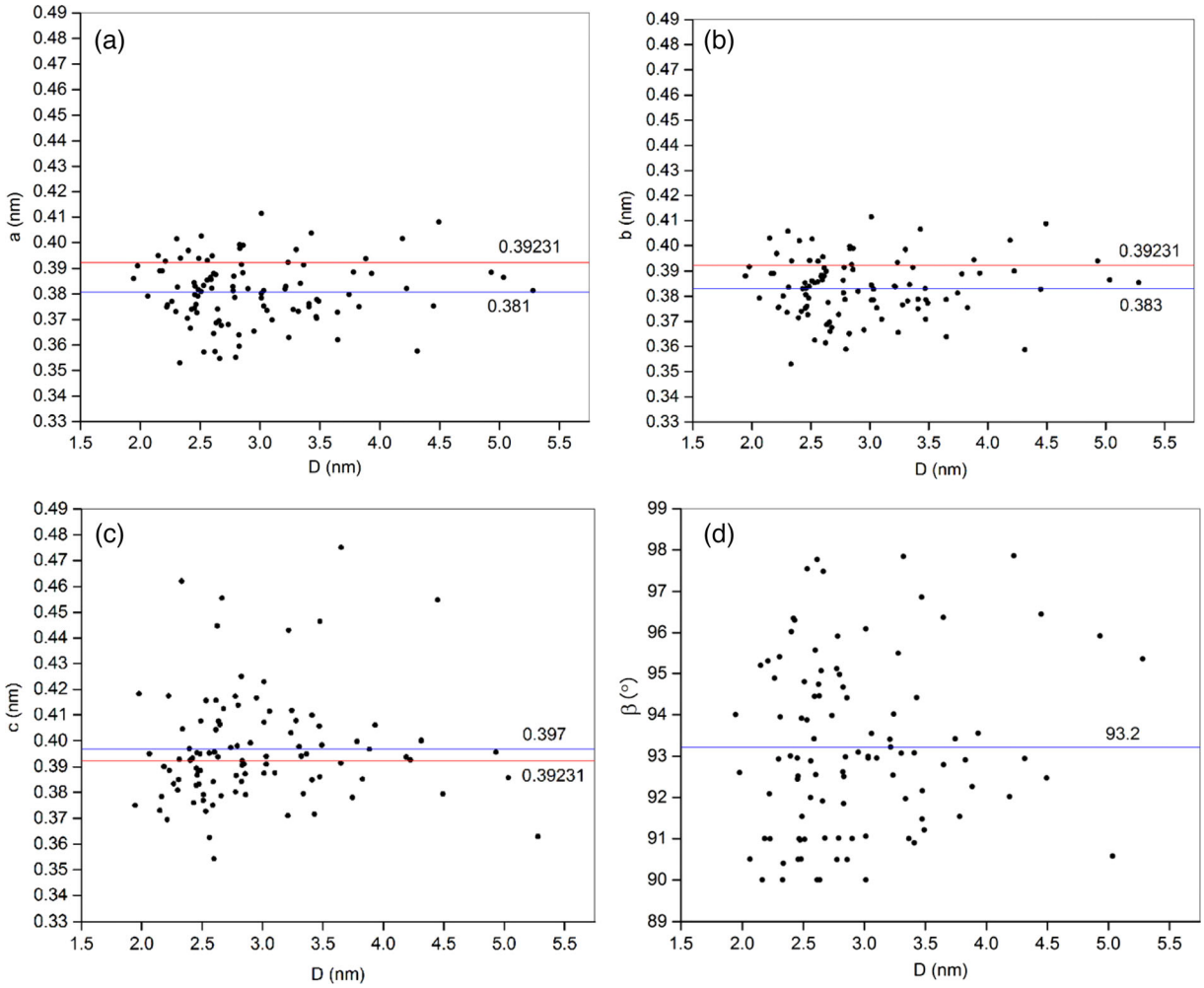


**Fig. 6** Distributions of the monoclinic lattice parameters **a** a, **b** b, **c** c, and **d** β plotted as a function of the Pt NP diameter

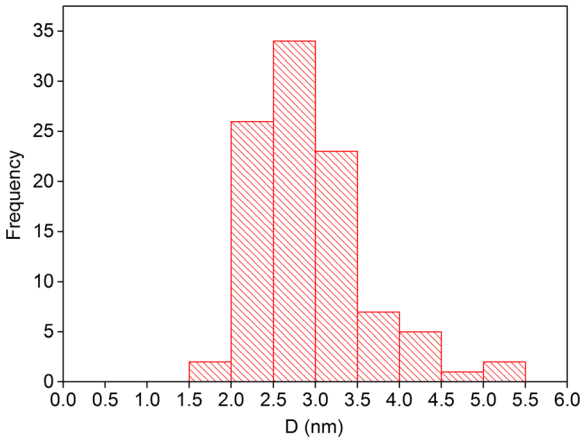


**Fig. 7** Histogram showing the diameter distribution of the Pt NPs used for the analysis of crossed lattice fringes

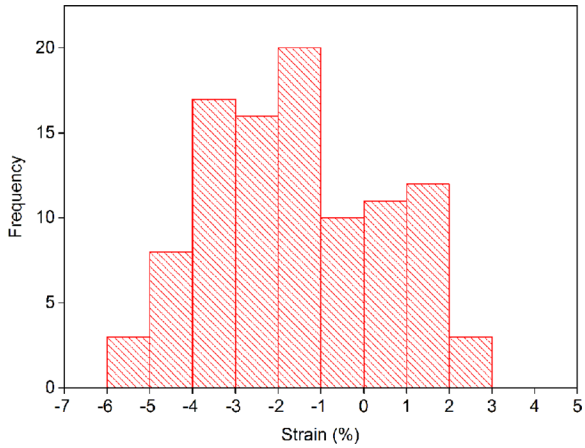


**Fig. 9** Lattice strain distribution of the Pt NPs deposited on the graphite particles

random anisotropic distortion of Pt NPs forms a variety of surface structures that can variously modify their catalytic activity. The strong scattering of *c* axis length also reflects the diversity of anisotropic strains.

In Fig. 8, the cube root of unit cell volume of the Pt NPs ($V^{1/3}$), which is ranging from 0.369 to 0.403 nm, was plotted as a function of particle diameter *D*. The mean value of $V^{1/3}$ is 0.386 ± 0.008 nm, which is ~1.6% smaller than that of bulk Pt.

Defining the lattice strain (%) as $100(V^{1/3} - a_0)/a_0$, where $a_0$ is the lattice constant of bulk Pt, the lattice strain of the Pt NPs ranges from a compression of 5.9% to an expansion of 2.8% as compared with bulk Pt. The expansion of lattice parameter is not limited to the current investigation of Pt NPs. Lattice constants larger than the bulk values were also reported in the case of Pd

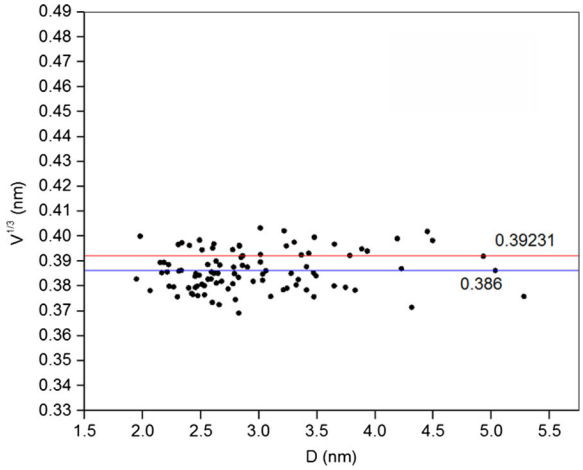


**Fig. 8** Monoclinic unit cell volume of the Pt NPs plotted as a function of diameter *D* (nm)

NPs (Heinemann and Poppa 1985; Giorgio et al. 1990). The distribution of lattice strain of the Pt NPs is shown in Fig. 9.

Among the 100 Pt NPs, 73 NPs are compressed and 27 NPs are expanded. The expanded volume of Pt NPs will enhance the surface reactivity of Pt NPs by upshifting the *d* states of Pt atoms (Mavrikakis et al. 1998). On the other hand, it has been reported that the ORR activity can be enhanced in the Pt NPs with a −2 to −3% surface strain on their (111) surfaces (Kattel and Wang 2014). Wang et al. (2013) also reported the enhanced ORR activity due to the shrinkage of Pt–Pt bond distances in the monolayer Pt shells prepared on Pd core nanoparticles.

The DFT calculation also supports the maximum ORR activity at a compressive strain of ~−2.3% (Strasser et al. 2010), which is very close to the average compressive strain of −2.5 ± 1.3% of the Pt NPs in the current experiment. Thus, it is considered that ~two-thirds of the Pt NPs with the compressive strains can exhibit higher ORR activities.

On the other hand, Bu et al. (2016) reported that the Pt (110) facets with large tensile strains are favorable for the optimization of Pt–O bond strength that affects the ORR activity. It was also reported that Pt {110} surfaces are more active than Pt {111} and {100} surfaces for the ORR in perchloric acid (Bu et al. 2016; Markovic et al. 1994).

A Pt NP with a size close to 2 nm was found out as shown in Fig. 10a. The optimized lattice constants for this particle are $a$ = 0.386 nm, $b$ = 0.388 nm, $c$ = 0.375 nm, and $\beta$ = 94.0°, where the unit cell volume $V$ is 0.0530 $nm^3$. Hence, the Pt NP has a large compressive bulk strain of −12.1%. Figure 10b shows a model of Pt particle composed of 206 atoms and has a size similar

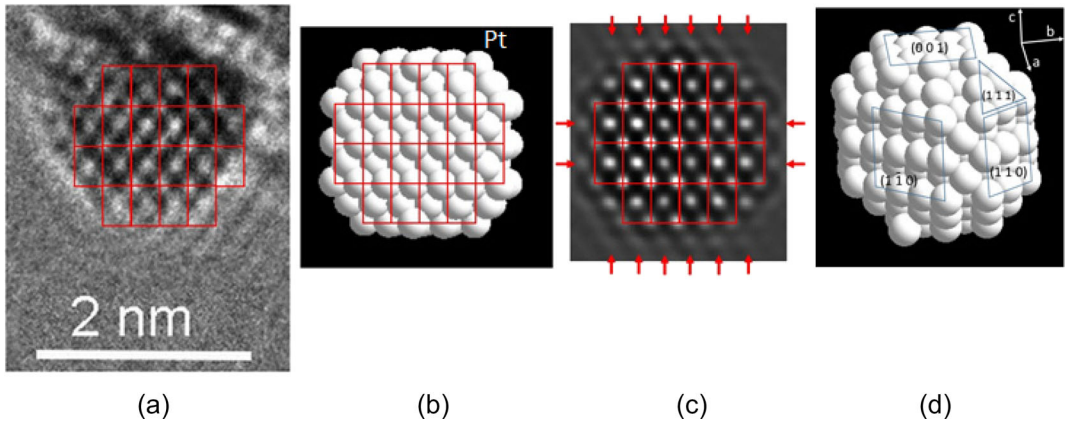


**Fig. 10** **a** HRTEM image of a Pt NP with a size close to 2 nm taken along a <110> zone axis. **b** Pt NP model with a size similar to **a**. **c** Calculated HRTEM image using the model of **b**. **d** Habit planes of the Pt NP model **b**. The *arrows* in **c** show ghost images

to Fig. 10a. Figure 10c displays a calculated HRTEM image that is closely resembling the image of Fig. 10a.

Assuming that the Pt NP of Fig. 10a is composed of 206 Pt atoms, the volume of the Pt NP was calculated to be 2.89 $nm^3$. Hence, the diameter of the Pt NP is estimated to be 1.8 nm, adopting a spherical model for the Pt NP. On the other hand, the particle diameter deduced from the area of HRTEM image was 1.9 nm. This good coincidence in the grain size estimation supports the appropriateness of the model. As displayed in Fig. 5a, the model of Pt NP (Fig. 10d) also suggests that most of the formed Pt NPs have the morphologies surrounded by the wider {110} top and bottom surfaces parallel to the surface (0001) planes of graphite particles and the narrower {110}, {111}, and {100} side surfaces.

Among the observed on-axis HRTEM images, approximately 90% of the crossed lattice images were along <110> zone axes. No on-axis <111> lattice images were found. This fact indicates that {110} crystal planes are most stably formed on the graphite particle surfaces by CAPD. As shown in Fig. 10d, the surface of Pt NP model is composed of four {110} planes, four {111} planes, and two {100} planes. The calculated surface energies of Pt are 1.68 $J/m^2$ for (110), 1.84 $J/m^2$ for (100), and 1.48 $J/m^2$ for (111) faces (Tran et al. 2016). The origin of the anisotropic strains observed in this study is not clear. One reason for the anisotropic distortion of unit cell, however, is considered to be due to the different surface energies that become more pronounced in the smaller particles of nanometer sizes. The strain generated at the Pt NP-graphite particle interface may induce the anisotropic distortion as reported in the study of substrate-induced strains at Pt NP-graphitized carbon black interfaces and Pt NP-$SnO_2$ interfaces (Daio et al. 2015).

As described above, the observed Pt NPs were anisotropically strained. No correlation was observed between the lattice parameters and the NP diameter. Approximately two-thirds of the Pt NPs were in the compressive state and ~one third of the Pt NPs were in the tensile state. It is expected that these differently strained states can contribute to the enhancement of the ORR activities of the Pt NPs prepared by CAPD.

## Conclusions

1. Pt NPs were prepared on graphite particles using CAPD. The Pt NPs exhibited thin plate-like morphologies, and the {110} crystal surfaces parallel to the (0001) planes of graphite particles were most frequently observed. The simulated image for a Pt NP model with top and bottom {110} surfaces well explained the observed HRTEM image of a Pt NP with a similar size.
2. The Pt NPs were found to be anisotropically deformed from the pristine fcc symmetry and were explained by the monoclinic structures whose lattice parameters were optimized by the least square method for 100 on-axis HRTEM images.
3. No correlation was observed between the monoclinic lattice parameters and the diameter of Pt NPs. Approximately two-thirds of the Pt NPs were compressively strained, and the other Pt NPs showed the expanded unit cells. The cube root of monoclinic unit cell of the Pt NPs varied from a compression of 5.9% to an expansion of 2.8% as compared with the bulk lattice constant of Pt.

**Acknowledgements** A part of this work was conducted at Advanced Characterization Nanotechnology Platform of the University of Tokyo, supported by "Nanotechnology Platform" of the Ministry of Education, Culture, Sports, Science and Technology (MEXT), Japan. This study is based on the results obtained from a project commissioned by the New Energy and Industrial Technology Development Organization (NEDO). The authors are grateful to Mr. Makoto Mori (TUS), Mr. Yuta Nakajo (TUS), Mr. Yorito Nishizawa (TUS), Mr. Kazuki Kasahara (TUS), and Ms. Yurie Inoue (TUS) for preparing the graphite particles with Pt NPs by CAPD.

**Compliance with ethical standards**

**Conflict of interest** The authors declare that they have no conflict of interest.

## References

Agawa A, Kunimatsu M, Ito T, Kuwahara Y, Yamashita H (2015) Preparation of Pt/C catalyst by coaxial arc plasma deposition for polymer electrolyte membrane fuel cells. ECS Electrochem Lett 4:F57–F60. doi:10.1149/2.0091510ee1

Berry CR (1952) Electron diffraction from small crystals. Phys Rev 88:596–599. doi:10.1103/PhysRev.88.596

Birringer R, Zimmer P (2009) Grain- and phase-boundary stress effects in nanocrystalline materials. Acta Mater 57:1703–1716. doi:10.1016/j.actamat.2008.11.040

Boswell FWC (1951) Precise determination of lattice constants by electron diffraction and variations in the lattice constants of very small crystallites. Proc Phys Soc Lond A 64:465–476. doi:10.1088/0370-1298/64/5/305

Bu L, Zhang N, Guo S, Zhang X, Li J, Yao J, Wu T, Lu G, Ma J-Y, Su D, Huang X (2016) Biaxially strained PtPb/Pt core/shell nanoplate boosts oxygen reduction catalysis. Science 354:1410–1414. doi:10.1126/science.aah6133

Daio T, Staykov A, Guo L, Liu J, Tanaka M, Lyth SM, Sasaki K (2015) Lattice strain mapping of platinum nanoparticles on carbon and $SnO_2$ supports. Sci Rep 5:13126. doi:10.1038/srep13126

Finch GI, Fordham S (1936) The effect of crystal-size on lattice-dimensions. Proc Phys Soc 48:85–94. doi:10.1088/0959-5309/48/1/312

Gholami R, Alyani M, Smith KJ (2015) Deactivation of Pd catalysts by water during low temperature methane oxidation relevant to natural gas vehicle converters. Catalysts 5:561–594. doi:10.3390/catal5020561

Giorgio S, Henry CR, Chapon C, Penisson JM (1990) Structure and morphology of small palladium particles (2-6 nm) supported on MgO micro-cubes. J Cryst Growth 110:254–260. doi:10.1016/0022-0248(90)90628-X

Heinemann K, Poppa H (1985) In-situ TEM evidence of lattice expansion of very small supported palladium particles. Surf Sci 156:265–274. doi:10.1016/0039-6028(85)90583-7

Hinokuma S, Murakami K, Uemura K, Matsuda M, Ikeue K, Tsukahara N, Machida M (2009) Arc plasma processing of Pt and Pd catalysts supported on $\alpha$-$Al_2O_3$ powders. Top Catal 52:2108–2111. doi:10.1007/s11244-009-9387-x

Kattel S, Wang G (2014) Beneficial compressive strain for oxygen reduction reaction on Pt (111) surface. J Chem Phys 141:124713-1–124713-8. doi:10.1063/1.4896604

Khatee S, Guerreo S, Su D, Darling RM, Protsailo LV, Shaoc M (2016) Fuel cell performance of palladium-platinum Core-Shell Electrocatalysts synthesized in gram-scale batches. J Electrochem Soc 163:F708–F713. doi:10.1149/2.1301607jes

Klimenkov M, Nepijko S, Kuhlenbeck H, Bfiumer M, Schlögl R, Freund H-J (1997) The structure of Pt-aggregates on a supported thin aluminum oxide film in comparison with unsupported alumina: a transmission electron microscopy study. Surf Sci 391:27–36. doi:10.1016/S0039-6028(97)00449-4

Lamber R, Wetjen S, Jaeger N (1995) Size dependence of the lattice parameter of small palladium particles. Phys Rev B 51:10968. doi:10.1103/PhysRevB.51.10968

Lennard-Jones JE, Dent BM (1928) The change in lattice spacing at a crystal boundary. Proc R Soc London A 121:247–259. doi:10.1098/rspa.1928.0194

Leontyev IN, Kuriganova AB, Leontyev NG, Hennet L, Rakhmatullin A, Smirnova NV, Dmitriev V (2014) Size dependence of the lattice parameters of carbon supported platinum nanoparticles: X-ray diffraction analysis and theoretical considerations. RSC Adv 4:35959–35965. doi:10.1039/c4ra04809a

Markovic NM, A ić RR, Cahan BD, Yeager EB (1994) Structural effects in electrocatalysis: oxygen reduction on platinum low index single-crystal surfaces in perchloric acid solutions. J Electroanal Chem 377:249–259. doi:10.1016/0022-0728(94)03467-2

Mavrikakis M, Hammer B, Nørskov JK (1998) Effect of strain on the reactivity of metal surfaces. Phys Rev Lett 81:2819. doi:10.1103/PhysRevLett.81.2819

Miyabayashi K, Miyake M (2016) Platinum nanoparticles modified with perfluorinated alkylamines as a model cathode catalyst for fuel cells. Electroanalysis 28:1–10. doi:10.1002/elan.201600625

Miyazawa K, Satsuki H, Kuwabara M, Akaishi M (2001) Microstructural analysis of high-pressure compressed $C_{60}$. J Mater Res 16:1960–1966. doi:10.1557/JMR.2001.0268

Qi WH, Huang BY, Wang MP, Yin ZM, Li J (2009) Molecular dynamic simulation of the size and shape-dependent lattice parameter of small platinum nanoparticles. J Nanopart Res 11:575–580. doi:10.1007/s11051-008-9392-1

Sepp S, Vaarmets K, Nerut J, Tallo I, Tee E, Kurig H, Aruväli J, Kanarbik R, Lust E (2016) Performance of polymer electrolyte membrane fuel cell single cells prepared using hierarchical microporous-mesoporous carbon supported Pt nanoparticles activated catalysts. Electrochim Acta 203:221–229. doi:10.1016/j.electacta.2016.03.158

Shao M, Peles A, Shoemaker K (2011) Electrocatalysis on platinum nanoparticles: particle size effect on oxygen reduction reaction activity. Nano Lett 11:3714–2719. doi:10.1021/nl2017459

Solliard C, Flueli M (1985) Surface stress and size effect on the lattice parameter in small particles of gold and platinum. Surf Sci 156:487–494. doi:10.1016/0039-6028(85)90610-7

Strasser P, Koh S, Anniyev T, Greeley J, More K, Yu C, Liu Z, Kaya S, Nordlund D, Ogasawara H, Toney MF, Nilsson A (2010) Lattice-strain control of the activity in dealloyed core–shell fuel cell catalysts. Nat Chem 2:454–460. doi:10.1038/NCHEM.623

Tran R, Xu Z, Radhakrishnan B, Winston D, Sun W, Persson KA, Ong SP (2016) Data descriptor: surface energies of elemental crystals. Scientific Data 3:160080. doi:10.1038/sdata.2016.80

Wang JX, Inada H, Wu L, Zhu Y, Choi Y, Liu P, Zhou W-P, Adzic RR (2009) Oxygen reduction on well-defined core-shell nanocatalysts: particle size, facet, and Pt shell thickness effects. J Am Chem Soc 131:17298–17302. doi:10.1021/ja9067645

Wang X, Orikasa Y, Takesue Y, Inoue H, Nakamura M, Minato T, Hoshi H, Uchimoto Y (2013) Quantitating the lattice strain dependence of monolayer Pt shell activity toward oxygen reduction. J Am Chem Soc 135:5938–5941. doi:10.1021/ja312382h

Zhang HY, Lu K, Hu ZQ (1995) Formation and lattice distortion of nanocrystalline selenium. Nanostruct Mater 6:489–492. doi:10.1016/0965-9773(95)00103-4

Zhang J, Vukmirovic MB, Xu Y, Mavrikakis M, Adzic RR (2005) Controlling the catalytic activity of platinum-monolayer electrocatalysts for oxygen reduction with different substrates. Angew Chem Int Ed 44:2132–2135. doi:10.1002/anie.200462335